CHEMISTRY OF MATERIALS

ARTICLE

pubs.acs.org/cm

Hydrogen Production via Chemical Looping Redox Cycles Using Atomic Layer Deposition-Synthesized Iron Oxide and Cobalt Ferrites

Jonathan R. Scheffe,[†] Mark D. Allendorf,[‡] Eric N. Coker,[§] Benjamin W. Jacobs,[‡] Anthony H. McDaniel,*[,‡] and Alan W. Weimer*[,†]

[†]Department of Chemical and Biological Engineering, 1111 Engineering Dr., ECCH 111, University of Colorado, Boulder, Colorado 80309-0424, United States

[‡]Sandia National Laboratories, Livermore, California 94551-0969, United States

[§]Sandia National Laboratories, Albuquerque, New Mexico 87123, United States

ABSTRACT: Iron oxide (γ-Fe_2O_3) and cobalt ferrite ($Co_xFe_{3-x}O_4$) thin films were synthesized via atomic layer deposition (ALD) on high surface-area (50 m^2 g^{-1}) m-ZrO_2 supports. The oxide films were grown by sequentially depositing iron oxide and cobalt oxide, adjusting the number of iron oxide to cobalt oxide cycles to achieve a desired stoichiometry. High resolution transmission electron microscopy and X-ray diffraction indicate that the films are crystalline and have a thickness of ~2.5 nm. Raman spectroscopy was used to confirm the predominance of the spinel phase in the case of cobalt ferrite. Films were chemically reduced at 600 °C using mixtures of H_2, CO, and CO_2. The evolution of oxide phases as a function of time during this reduction was observed using in situ X-ray diffraction, showing that γ-Fe_2O_3 are reduced only to FeO, while $Co_xFe_{3-x}O_4$ are reduced all the way to a Co/Fe alloy. Subsequent water splitting measurements in a stagnation flow reactor yielded peak H_2 rates exceeding virtually all of those reported in the literature. $Co_{0.85}Fe_{2.15}O_4$ films were successfully cycled without deactivation and produced four times more H_2 than γ-Fe_2O_3 films principally because of the deeper chemical reduction possible. Together, these results suggest a path to robust materials for chemical looping cycles and thermal gas splitting. They also indicate that ALD films can serve as an effective platform for probing the surface chemistry of these processes, since they maintain their reactivity at these temperatures, in contrast with oxide powders that are deactivated by sintering and grain growth.

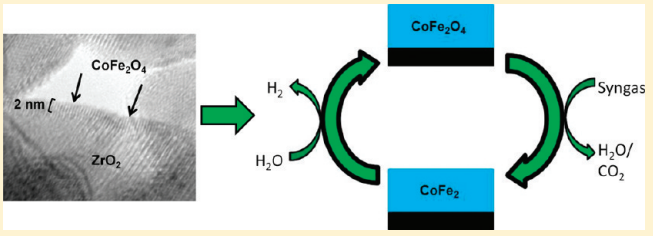

KEYWORDS: water splitting, hydrogen, ferrite, atomic layer deposition, film, thermochemical cycle

INTRODUCTION

Iron oxide and metal-substituted ferrites ($M_xFe_{3-x}O_4$) are attracting considerable interest for use as intermediates in chemical looping processes[1,2] and thermal redox cycles for the renewable production of H_2 in concentrated solar power applications.[3−5] In addition, these metal oxides can be used as catalysts for the decomposition of NO_x,[6,7] organic contaminants,[8,9] decomposition of biomass tars,[10] and for the production of H_2 via the water gas-shift reaction.[11,12] Their magnetic properties also make them an attractive catalyst support since they facilitate downstream separation in large-scale environmental catalysis applications.[13]

Achievement of a detailed understanding of the mechanisms and rate-limiting steps, and the practical development of such processes, are often hindered by morphological instabilities that exist in ferrite powders and dense composites. For example, Bleeker et al., using iron oxide particles in a two-step redox cycle to produce H_2 from steam,[14,15] observed grain growth with increased cycling leading to decreased surface area and ultimately to reduced conversion efficiency. Similar behavior was observed by Bohn et al. when fully reducing iron oxide particles to metallic iron in a packed bed reactor.[2] In this case, however, deactivation was abated when the iron oxide was only partially reduced to the wustite phase (FeO). Ferrite-based thermal gas splitting cycles operating at high temperature (1400−1600 °C) suffer from similar issues. In this case, Fe^{3+} ions are thermally reduced to Fe^{2+} and then reoxidized by H_2O or CO_2 to produce H_2 or CO. Steinfeld et al. showed that CO_2 gas splitting by reaction with FeO particles depends strongly on surface area and attributed this to a rate-limiting surface chemical reaction.[16] In addition, Weidenkaff et al. observed an FeO particle size dependence on H_2O splitting, and concluded this is due to bulk diffusion limitations.[17] In an effort to eliminate sintering problems that effectively shut down the gas splitting reaction, ferrites deposited on porous support materials such as SiO_2, Al_2O_3, ZrO_2, and yttria-stabilized zirconia (YSZ) were proposed by several investigators.[3,4,18,19] However, these supports are not always chemically inert, as Kodama et al. subsequently observed of ZrO_2 supports, further complicating the mechanistic picture.[20] These results make it clear that a versatile material platform, in which the oxide morphology and composition are stable and can be controlled, would be highly advantageous for probing the kinetics of these high-temperature metal-oxide processes. In addition, such a platform would have significant practical

Received: August 12, 2010
Published: March 24, 2011

dx.doi.org/10.1021/cm103622e | *Chem. Mater.* 2011, 23, 2030–2038

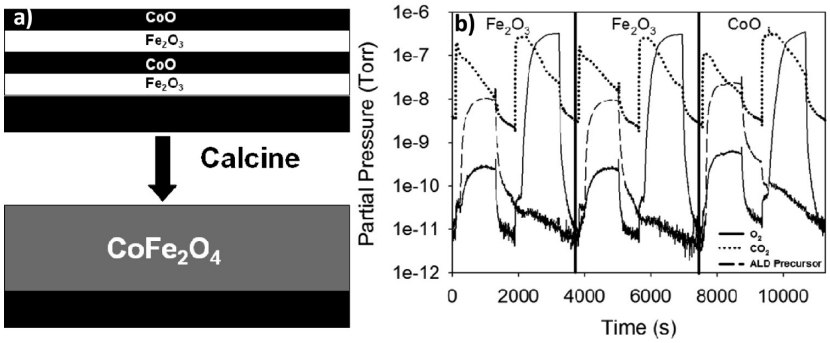

Figure 1. (a) Schematic of $CoFe_2O_4$ synthesis process by ALD, and (b) corresponding in situ mass spectrometry results showing Fe_2O_3 and CoO deposition cycles.

advantages if a high surface area can also be achieved to increase conversion efficiencies and reaction rates.

Thin films deposited by atomic layer deposition (ALD) have the potential to meet these requirements. Unlike solution and line-of-sight methods used to synthesize metal-substituted ferrites, including solution combustion synthesis,[6] aerial oxidation of aqueous suspensions,[5] sol−gel process,[8] laser molecular beam epitaxy,[21] sputtering,[22] and chemical vapor deposition (CVD),[23] ALD can produce conformal thin films on porous materials. Because of the self-limiting nature of ALD chemistry, precursors of one-half-reaction react only on the surface with intermediate functional groups generated by the other precursor. This ensures atomic level control, since at most one submonolayer is deposited per half-reaction; it also allows film thickness to be accurately controlled. Growth of cobalt oxide films is accessible by ALD and has been achieved on a wide array of surfaces using precursors such as bis(*N*,*N*′-diisopropylacetamidinato)cobalt(II),[24] CoI_2,[25] and $Co(thd)_2$.[26,27] Similarly, iron oxide films have been deposited using bis(*N*,*N*′-diisopropylacetamidinato)iron(II),[24] $Fe(acac)_3$,[28] $Fe(thd)_2$,[29] $Fe(thd)_3$,[30] iron(III) *tert*-butoxide,[31] and ferrocene.[32,33] As a result, various $Co_xFe_{3-x}O_4$ stoichiometries can be deposited by combining selective organometallic precursors in alternating doses of correct proportions.[34]

Here, we describe the development of an ALD-based platform for probing high-temperature metal-oxide redox cycles. We then demonstrate production of H_2 via a water-splitting (WS) redox cycle and measure the reaction rate as a function of time and number of reaction cycles. Growth of nanoscale ($\leq$10 nm) Fe_2O_3 and $Co_xFe_{3-x}O_4$ films on high surface-area monoclinic ZrO_2 supports (50 m^2 g^{-1}) was achieved using ferrocene and cobaltocene as the iron and cobalt sources and O_2 as the oxidant. Mass loadings up to 37 wt % were achieved while maintaining a gas-permeable structure. The resulting materials have relatively stable microstructures up to 600 °C. These properties allow them to be used in a variety of chemical looping and thermal redox cycles at reasonable conversion rates without the progressive loss of surface area that occurs in some materials and ultimately limits efficiency and lifetime. An additional advantage is that surface-limited gas splitting kinetics can be probed, since bulk and/or grain-boundary diffusion limitations that rapidly develop with powders or nonporous solids is significantly mitigated.

Water splitting was achieved by first chemically reducing the films in a synthesis gas atmosphere, then exposing them to steam to form H_2 and regenerate either Fe_3O_4 or $Co_xFe_{3-x}O_4$. A key finding is that the peak, mass-normalized H_2 production rates are nearly an order of magnitude faster at 600 °C than virtually all previously reported oxide materials, clearly demonstrating the advantage of this platform. In addition, we find that the $Co_xFe_{3-x}O_4$ ALD films yield significantly more H_2 than ALD-deposited Fe_2O_3 (a factor of 2 or more) because of the formation of a stable redox-active Co−Fe alloy in the fully reduced state. These results represent a major improvement over traditional materials used in thermal gas splitting redox cycles and suggest a path toward the development of effective materials for solar driven fuel production. They also demonstrate that these novel materials are an effective, tunable platform for fundamental investigations of gas splitting, from which much-needed kinetic data can be obtained.

MATERIALS AND METHODS

ALD Synthesis. Multilayers of iron(III) oxide and cobalt(II) oxide were deposited on porous m-ZrO_2 substrates (Brunauer−Emmett−Teller (BET) surface area = 50 m^2 g^{-1}, Alfa Aesar) via ALD in alternating cycles according to the schematic shown in Figure 1a. Details of the reactor configuration are described elsewhere.[33] The zirconia supports were ground with a mortar and pestle and sieved to particle sizes in the range 149−250 μm to facilitate gas diffusion through the entire porous structure and achieve conformal coverage of the deposit. Growth occurred at 450 °C and at a reaction pressure of 200 mTorr.

Iron(III) oxide deposition consisted of flowing ferrocene (99% purity, Alfa Aesar) or high purity oxygen (99.9%) into the reactor, with each dose representing one-half of the ALD cycle. A saturated vapor of ferrocene in nitrogen was delivered through a 200 mL bubbler (Precision Fabricators Ltd.) heated to 60 °C. The reactor was then purged with pure nitrogen to remove any unreacted ferrocene and vapor-phase byproducts of the ALD chemistry. Subsequently, oxygen was introduced into the reactor followed by a second nitrogen purge. Layers of cobalt(II) oxide were deposited in an identical manner to that of iron(III) oxide using cobaltocene as the organometallic precursor.

In situ mass spectrometry was used to monitor the extent of reaction, as is commonly done.[35,36] A plot illustrating the self-limiting nature of the ALD chemistry is shown in Figure 1b. Each half reaction for both Fe_2O_3 and CoO deposition is clearly observed. Fe_2O_3 is deposited in the first two cycles and is characterized initially by an increase in the CO_2 partial pressure resulting from a reaction between ferrocene and the oxide surface. Once the deposition nears completion, a mass spectral feature associated with the organometallic precursor at an m/e = 65 increases as the unreacted ferrocene breaks through the reaction zone. The partial pressure of CO_2 also begins to decrease at this point. Following a nitrogen purge the surface is oxidized with O_2 and an increase in CO_2, which is also a byproduct of this half reaction, is

dx.doi.org/10.1021/cm103622e |*Chem. Mater.* 2011, 23, 2030–2038

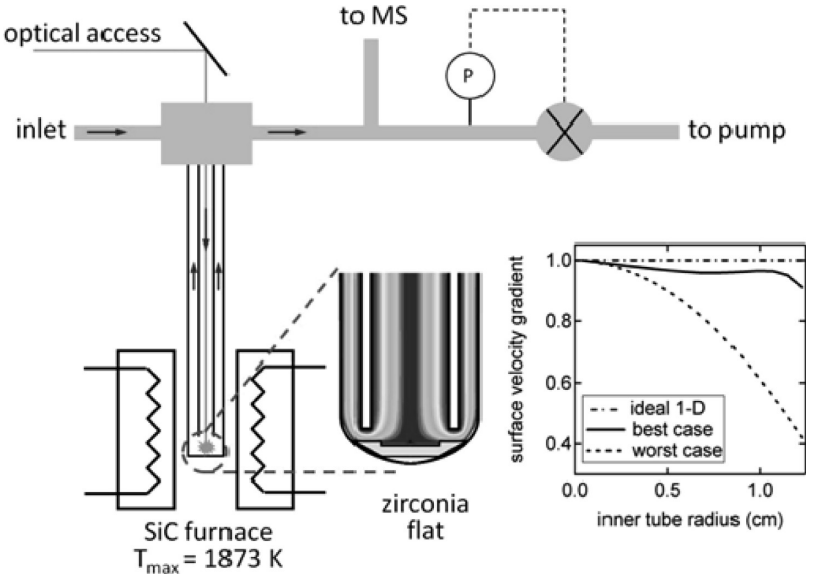

Figure 2. Schematic of the stagnation flow reaction (SFR). Transport gradients are independent of inner tube radius out to 1.0 cm.

observed. Once O_2 breakthrough is achieved, indicating a termination of the half reaction, CO_2 again decreases. This process is repeated with ferrocene for one more cycle, shown in the center segment of Figure 1b, and then CoO is deposited using cobaltocene. The CoO ALD chemistry is nearly identical to that of ferrocene, evidenced by similar temporal behavior of the precursor and byproduct spectral patterns.

Material Characterization. Electron microscopy was used to characterize morphology and crystallinity of the as-deposited ALD films, using a JEOL 2010F field-emission transmission electron microscope (HRTEM) operating at 200 kV. The coated support material was lightly crushed using a mortar and pestle, then sonicated in ethanol. Copper TEM grids with a thin carbon support film were dipped into the suspension and allowed to dry. A JEOL 7600F field-emission scanning electron microscope (FESEM) operating at 4 kV and 15 kV was also used to examine surface morphology and local chemical variation. Here, samples were mounted on conductive tape and sputtered with carbon. Elemental composition was determined via energy dispersive X-ray spectroscopy (EDS) in the FESEM, and induced coupled plasma−atomic emission spectroscopy (ICP-AES). Surface areas were determined using a Micrometrics Gemini V BET surface area analyzer.

A Raman microscope was used to interrogate phonon modes in the films to fingerprint the chemical structure of the deposits. Spectra were acquired ex situ in a 180° backscattering geometry using a 100× objective lens and 532-nm excitation from a frequency-doubled Nd:YAG laser. The scattered light was filtered by a film polarizer in crossed polarization with the incident, linearly polarized light to reduce the non-Raman background. A Semrock edge filter was used to reject the elastically scattered light. A spectrograph with a single 1200 groove mm^{-1} grating dispersed the light onto a CCD detector cooled by liquid nitrogen. The laser has a spot size of approximately 1 μm, and Raman spectra were collected at multiple locations on the sample surface. The spectrometer was calibrated with a neon lamp.

High-temperature X-ray diffraction (HT-XRD) experiments were performed using a Scintag PAD X diffractometer (Thermo Electron Inc.; Waltham, MA). This diffractometer is equipped with a sealed-tube source (Cu Kα, λ = 0.15406 nm), an incident-beam mirror optic, a peltier-cooled Ge solid-state detector, and a Buehler hot-stage with Pt/Rh heating strip and surround heater. The hot stage lies within a sealed cell with X-ray-transparent beryllium windows, and is operable from ambient temperature to 1600 °C, and at gas pressures from 10^{-9} to 10^{3} Torr. A gas manifold was attached to the inlet of the reaction cell allowing the controlled flow of helium, hydrogen, and carbon dioxide through the cell. Suitable gas compositions were achieved using mass flow controllers (Brooks Instruments).

In situ HT-XRD experiments were conducted at atmospheric pressure under gas flow rates of 500 sccm. Samples of typically 20−30 mg material were analyzed as thin layers (ca. 50−100 μm) of powder on top of single-crystal ⟨100⟩ 9 mol.-% yttria-stabilized zirconia (YSZ) platelets (10 mm × 10 mm × 0.5 mm, MTI Corporation). Experiments involved purging the reaction cell with He, then ramping the temperature to 600 °C before switching to a reducing gas mixture (2340 ppm H_2 and 2340 ppm CO_2). Diffraction patterns were recorded at room temperature and at 600 °C under He, and then continuously at 600 °C for 2−4 h after introducing the reducing gas. A final XRD pattern was recorded after cooling the sample to ambient temperature. Heating and cooling ramp rates were set to 20 °C min^{-1}. Using this experimental configuration, phase fractions as low as approximately 1 wt % can be reliably detected. Temperature calibration was performed using the thermal expansion behavior of known materials (e.g., alumina or Pt) to an accuracy of ±5 °C. Diffraction patterns were collected at 40 kV and 30 mA using fixed slits and a count time of 1 s.

Stagnation Flow Reactor. Samples were reduced and oxidized in a stagnation flow reactor (SFR) shown in Figure 2. The reactor consists of a stainless steel gas-handling manifold, ceramic reactor core, high temperature furnace (Carbolite STF16/180), and modulated effusive beam mass spectrometer. The ceramic reactor core is configured to allow inlet gases flowing downward toward the round-bottom, closed end of an Al_2O_3 tube (McDanel Advanced Ceramic Technologies) to impinge on a zirconia disk. Gases then turn 180° and exit via an annular space between the walls of two concentric tubes (see cross sectional view and flow stream lines in Figure 2). The distance between the zirconia disk and bottom of the inner tube wall was maintained at 8 mm to ensure ideal stagnation flow behavior, as determined by two-dimensional (2-D) computational fluid dynamic (CFD) calculations. The gas-phase region above the zirconia disk between centerline and inner tube radius can be considered an ideal one-dimensional (1-D) stagnation plane governed by diffusive transport. Plots of the surface velocity gradient as a function of inner tube radius are shown in the inset to Figure 2 for (1) an ideal 1-D case; (2) the best-case CFD prediction used to determine the reactor geometry; and (3) a worst-case scenario. It is important to note that the

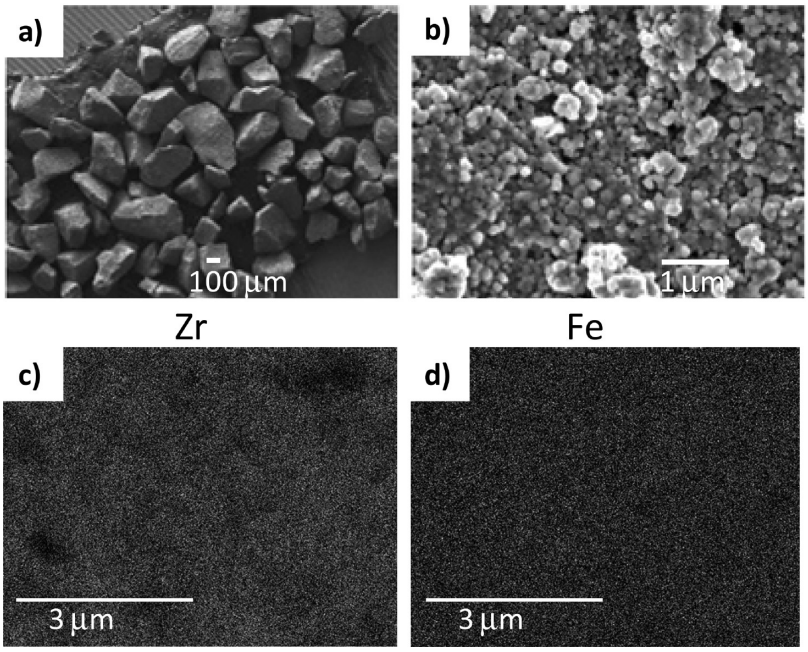

Figure 3. (a) FESEM image of bulk m-ZrO_2 supports at low magnification, (b) FESEM image of m-ZrO_2 nanoparticles within the bulk support, (c) EDS Zr map after $Co_{0.85}Fe_{2.15}O_4$ deposition, and (d) EDS Fe map after $Co_{0.85}Fe_{2.15}O_4$ deposition.

SFR operates in a flow regime where velocity and thermal gradients are independent of tube radius, such that materials sitting on the zirconia disk experience a uniform gas composition.

Gases exiting the flow reactor were sampled using a differentially pumped, modulated effusive beam mass spectrometer (Extrell C50, 500 amu). Upon expansion into the second of three pumping stages, the molecular beam is chopped by a resonant modulator driven at 200 Hz and ionized by electron impact at 30 eV. Modulated ion current from the electron multiplier is routed through a lock-in amplifier to discriminate against DC background. This increases detector sensitivity and digitally filters ion current resulting from gases that persist in the ionization volume (a significant issue when using water vapor and producing H_2), thus enabling real-time baseline correction and a higher degree of precision for quantifying component partial pressures. A mixture of 5 vol % CO and 5 vol % H_2 in He was used to calibrate the detector.

Mass flow controllers were used to meter all gas feed rates. The reactor exhaust was throttled, allowing for feedback control of the reactor pressure to any desired set point within the range 1−760 Torr. Unless otherwise indicated, chemical reduction and WS reactions were conducted at a temperature of 600 °C and a total flow rate of 500 sccm, using mixtures of H_2, CO, CO_2, H_2O, and He at a total pressure of 75 Torr. Water was delivered through an evaporator fed by a microsyringe pump. Liquid nitrogen traps were used to condense H_2O prior to sampling the reactor effluent with the mass spectrometer. Between 50−200 mg of crushed and sieved ALD-coated m-ZrO_2 support were placed in the reactor. Chemical reduction was accomplished by exposing the sample to a gas mixture of 1 vol % H_2, 1 vol % CO, and 2 vol % CO_2 diluted in He for a total of 600 s. The CO_2 signal at m/z = 44 was monitored to determine a point at which full reduction was achieved. WS was performed using 5−6 vol % steam in He over a 600 s total reaction time.

RESULTS AND DISCUSSION

ALD Materials. ALD films with three representative stoichiometries (x = 0, 0.67, and 1 in $Co_xFe_{3-x}O_4$) were prepared by adjusting the number and sequence of iron oxide and cobalt oxide deposition cycles as described previously (e.g., 1 cobalt oxide cycle for every 2 iron oxide cycles in $CoFe_2O_4$). Mass loading was controlled by limiting the total number of ALD cycles. For example, 24 cycles produces a loading of 20 wt %, while 50 cycles yields 37 wt %. The exact film composition was determined using ICP-AES and agreed well with the targeted stoichiometries based on Fe and Co cycle combinations, indicating that both iron oxide and cobalt oxide growth rates are similar and that ALD reactions had gone to completion.

Electron microscopy and surface area measurements demonstrate the stability of the support microstructure at ALD conditions used here. FESEM images of $Co_{0.85}Fe_{2.15}O_4$ deposited on 50 $m^2\ g^{-1}$ supports are presented in Figures 3a and 3b. The bulk support was ground and sieved prior to ALD and, at ×40 magnification, appears to have an average particle size of order 200 μm. The high surface area of these ceramic supports is the result of sintering zirconia nanoparticles with primary diameters of nominally 50 nm, as seen at higher magnification (×20000) in Figure 3b. Measurements of the specific surface area of the supports using BET methods confirm that significant sintering or grain growth does not occur during ALD. After $Co_{0.85}Fe_{2.15}O_4$ deposition (37 wt % loading), the surface area of the support decreased from 51 to 28 $m^2\ g^{-1}$. This decrease agrees well with the increase in mass because of the addition of the ferrite film, and also confirms that deposition does not result in pore clogging. EDS mapping of Zr and Fe (Figure 3c and 3d) show that iron is uniformly distributed throughout the support.

TEM analysis reveals the crystalline nature of the m-ZrO_2 nanoparticles in the support, as well as the deposited $Co_{0.85}Fe_{2.15}O_4$ film. TEM and HRTEM images of the uncoated m-ZrO_2 support are shown in Figures 4a and 4b. The lattice fringes are clearly observed in Figure 4b, and the accompanying electron diffraction pattern (inset Figure 4a) confirms that the nanoparticles making up the support are m-ZrO_2. TEM images in Figures 4c and

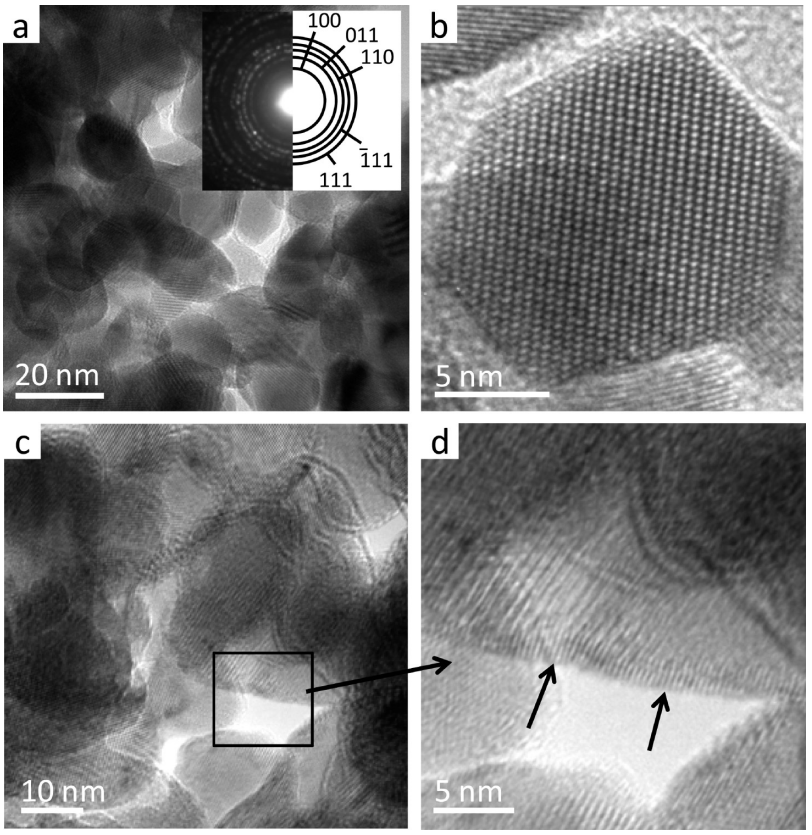

Figure 4. (a) HRTEM image of m-ZrO_2 support and corresponding diffraction pattern, (b) HRTEM image of m-ZrO_2 nanoparticle within support, (c) HRTEM image after $Co_{0.85}Fe_{2.15}O_4$ deposition, and (d) HRTEM image showing crystalline $Co_{0.85}Fe_{2.15}O_4$ film on m-ZrO_2.

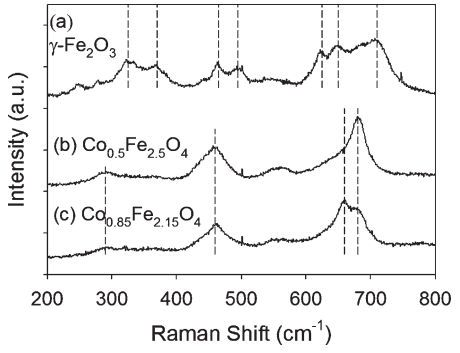

Figure 5. Raman spectra of (a) γ-Fe_2O_3 deposited on m-ZrO_2, (b) $Co_{0.5}Fe_{2.5}O_4$ deposited on m-ZrO_2, and (c) $Co_{0.85}Fe_{2.15}O_4$ deposited on m-ZrO_2.

4d show that a thin film surrounds the m-ZrO_2 nanoparticles after deposition. This is evidenced by a 2 nm thick layer which has a different crystallographic orientation than the underlying support. This interface is not observed for the uncoated zirconia. Electron energy loss spectroscopy (EELS) also shows cobalt and iron oxides present on the surface of the support particles.

The chemical structure and homogeneity of the films were established by Raman spectroscopy. The strongest Raman modes observed for ALD iron oxide films occur at 325, 370, 465, 495, 625, 650, and 710 cm^{-1}, as shown in Figure 5a. These modes are indicative of maghemite (γ-Fe_2O_3) and agree well with previous literature reports.[37,38] This is also indirect confirmation for the presence of a nanoscale thin film as maghemite is the more thermodynamically favored phase of Fe^{3+} for small particle sizes (less than 16 nm) because it possesses a lower surface energy than hematite.[37,39,40]

The Raman spectra also provide indirect evidence for conformal coverage of the ALD films on the support because no modes indicative of m-ZrO_2 are evident. Substitution of cobalt for iron in the ALD film leads to a decrease in the Raman modes associated with maghemite and an increase in the intensity of magnetite (Fe_3O_4) modes at 290, 460, and 680 cm^{-1} (Figure 5b).[37,41] In addition, the peak at 680 cm^{-1} is asymmetric, which is expected for pure Fe_3O_4 and is attributable to the presence of Co substituted for Fe. As the cobalt stoichiometry in the film increases from 0.5 to 0.85, a new peak at 660 cm^{-1} appears. This observation is consistent with an inverse spinel structure, in which Co substitutes for Fe in octahedral sites.[23,41]

Chemical Reduction and HT-XRD. Iron oxide and cobalt ferrite samples were chemically reduced in either a 1:1 mixture of H_2:CO_2 diluted in He or a 1:1:2 mixture of H_2:CO:CO_2 diluted in He. By including CO_2 in the reducing gas, the formation of metallic iron (Fe^0) can be suppressed when starting from Fe_2O_3 (Fe^{3+}), such that the formation of FeO (Fe^{2+}) is thermodynamically favored. This is discussed in detail by Bohn et al.,[2] whose results we confirmed with thermodynamic equilibrium calculations performed using the software package FactSage.[42] Bohn et al. report better redox cycle repeatability when partially reducing Fe_2O_3 particles to FeO, which they attributed to suppression of grain growth and sintering. Therefore, we chose to chemically reduce our materials to minimize cycle-to-cycle

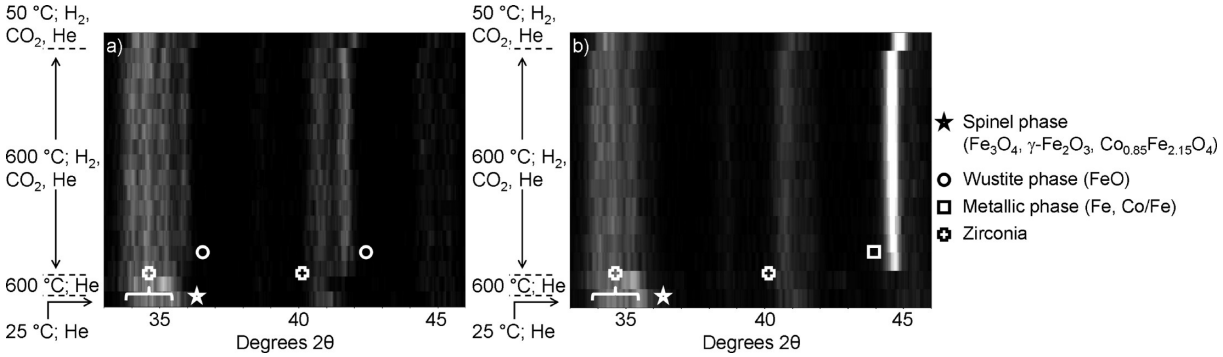

Figure 6. In situ XRD spectra of samples reduced in 1 vol % H_2/1 vol % CO_2 in He (500 sccm total) at 600 °C. (a) Fe_2O_3 on m-ZrO_2 (ALD/20.2% mass loading). (b) $Co_{0.85}Fe_{2.15}O_4$ on m-ZrO_2 (ALD/19% mass loading). Chemical reduction occurred at 600 °C for 148 min.

variability in H_2 production rates, as well as to enable us to probe WS chemistry on FeO surfaces.

The formation of various metal oxide phases as a function of reaction time and reducing-gas atmosphere was measured in situ by X-ray diffraction. During chemical reduction of ALD γ-Fe_2O_3 thin films the FeO phase persists for up to 148 min, which is in agreement with both our thermodynamic calculations and reports by Bohn et al. As shown in Figure 6a, after exposure to the reducing atmosphere there is an immediate appearance of FeO (42° 2θ), and the trace intensity for maghemtite (35° 2θ) decreases. By the end of the experiment, no changes in either γ-Fe_2O_3 or FeO trace intensity are observed, indicating that the reaction is complete. The reduction to FeO likely proceeds through an intermediate Fe_3O_4 oxide phase; however, evidence for this transition is difficult to verify at the instrument resolution used in this particular experiment because of overlap in the Fe_3O_4 and γ-Fe_2O_3 XRD patterns and interference from m-ZrO_2.

Although the chemical reduction of Fe_2O_3 and Fe_3O_4 to FeO has been reported previously, the chemical reduction of iron to Fe^{2+} in cobalt ferrites has not been investigated. Consequently, we modeled the reaction using thermodynamic equilibrium calculations, assuming conditions conducive to the formation of FeO from Fe_2O_3. These calculations predict the formation of metallic Co and Fe, and no conditions could be found for which a thermodynamically stable phase of Fe^{2+} exists in the presence of the $H_2/CO/CO_2$ reduction mixture. In agreement with these results, we find experimentally that Fe^{2+} does not form when ALD-$Co_{0.85}Fe_{2.15}O_4$ is reduced. Instead, in the presence of the reducing gas mixture, there is a rapid transition to a Co/Fe alloy (44.5° 2θ) as seen in Figure 6b. Binary Co−Fe phase diagrams predict that this alloy, rather than separate Co and Fe phases, is the thermodynamically stable phase under these conditions.[43,44] While the intensity of the alloy peak slowly increases during the reaction, the conversion is nearly complete almost immediately after reducing gases are delivered. As will be discussed in the next section, deeper reduction of the cobalt ferrite films leads to a higher yield of H_2 by WS relative to ALD γ-Fe_2O_3 because the Co/Fe alloy is redox active and can be cycled.

Water Splitting in the Stagnation Flow Reactor. The temporal WS behavior of the two ALD materials (Figure 7) illustrates the potential for rapid, high yield, and reproducible redox or chemical looping using this material platform. Hydrogen production rates measured on chemically reduced ALD γ-Fe_2O_3 (20.2 wt %) and ALD-$Co_{0.85}Fe_{2.15}O_4$ (19.0 wt %) at 600 °C are presented in Figures 7a and 7b. Time-dependent H_2 evolution is characterized by an initial rapid rise to a peak rate, followed by an exponential decay. This suggests that the rate-limiting step is a chemical reaction, not diffusion, because a $t^{-0.5}$ behavior is expected from a core−shell model of a diffusion-limited reaction.[45]

Upon cycling, the peak H_2 production rate observed for ALD γ-Fe_2O_3 decreases from 36.9 to 31.1 μmol s^{-1} g^{-1} over the course of five redox cycles. The drop in peak H_2 production rate is accompanied by a ~55% decrease in the total amount of H_2 produced (see Table 1) and a similar decrease in the time required to achieve 95% conversion, suggesting a loss of accessible iron in this material. This is consistent with BET surface area measurements, which indicate a 30% decrease from 39 to 27 m^2 g^{-1}. These changes occur relatively quickly, however (within 4 cycles), after which total production is stable.

The ALD-$Co_{0.85}Fe_{2.15}O_4$ (19 wt %) film is more robust with respect to cycling than ALD γ-Fe_2O_3. As seen in Figure 7b and Table 1, the peak H_2 production rates are virtually unchanged from cycle 1 to cycle 5, and the total H_2 production decreases by only 6%. This is in spite of the fact that the BET surface area decreases somewhat (from 41 to 31.5 m^2 g^{-1}) over the five cycles, which is comparable to the decrease observed for the ALD γ-Fe_2O_3 films. An additional noteworthy point is that, even though ALD-$Co_{0.85}Fe_{2.15}O_4$ is reduced to metallic Co/Fe prior to WS, as evidenced by the in situ XRD experiments (Figure 6), it does not lose activity as does Fe_2O_3 when reduced to Fe metal.[2,15] The change in surface area probably results from a small amount of sintering that occurs in the porous ZrO_2 at this temperature, indicating this support is near its high-temperature limit. However, it also indicates that loss of surface area is not the cause of the decrease in H_2 production capacity exhibited by ALD γ-Fe_2O_3. The reason for the superior performance of the ALD-$Co_{0.85}Fe_{2.15}O_4$ is thus unclear, although it appears that cobalt has the effect of limiting the migration of iron, thereby hindering its ability to diffuse and sinter. The in situ XRD data give no indication that either Fe or Co is dissolving in the support, so it appears that Co influences surface processes. It is also apparent that, unlike ALD γ-Fe_2O_3, the H_2 production rate does not return to zero during the course of the experiment as the rate plateaus at 400 s. This may be due to very slow oxidation of Co or surface-catalyzed decomposition of H_2O that continuously produces small amounts of H_2.

The total H_2 yield for ALD-$Co_{0.85}Fe_{2.15}O_4$ (19 wt %) is greater than ALD γ-Fe_2O_3 for the 7 redox cycles examined (Table 1). The initial ALD-$Co_{0.85}Fe_{2.15}O_4$ H_2 yield is approximately 4200 μmol g^{-1}, whereas the initial yield for ALD γ-Fe_2O_3 is 1800 μmol g^{-1}. The total H_2 produced by the ALD cobalt ferrite also

dx.doi.org/10.1021/cm103622e |Chem. Mater. 2011, 23, 2030–2038

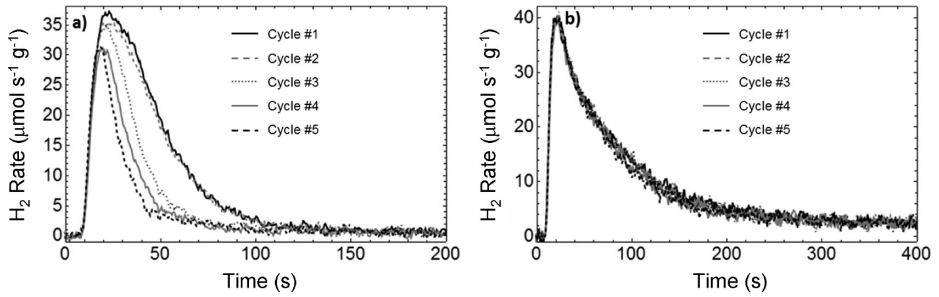

Figure 7. H_2 production rates as a function of time for five cycles of samples reduced in 1 vol % CO/1 vol % H_2/2 vol % CO_2 in He (500 sccm total). (a) Fe_2O_3 (ALD/20.2% mass loading); (b) $Co_{0.85}Fe_{2.15}O_4$ (ALD/19% mass loading).

Table 1. Peak H_2 Rates and Corresponding Total H_2 Yields for ALD-Coated m-ZrO_2 after Reduction in 1 vol % CO/1 vol % H_2/2 vol % CO_2 in He (500 sccm total)

	total H_2 produced (μmol g^{-1})		peak H_2 production rate (μmol s^{-1} g^{-1})	
cycle number	$Co_{0.85}Fe_{2.15}O_4$ ALD	Fe_2O_3 ALD	$Co_{0.85}Fe_{2.15}O_4$ ALD	Fe_2O_3 ALD
1	4154.5	1760.4	38.9	36.9
2	4131.2	1686.5	40.1	35.1
3	3976.7	1191.5	40.0	34.8
4	3877.0	895.7	39.4	30.9
5	3893.8	796.4	39.3	37.0
6	3652.2	815.8	36.5	31.1
7	3927.6	835.5	39.3	29.3

remains stable for all cycles, whereas that of the ALD γ-Fe_2O_3 cycled at 600 °C stabilizes at approximately 800 μmol g^{-1} by the fifth cycle, representing a 55% drop from the initial H_2 yield. Differences in the total amounts of hydrogen produced between ALD cobalt ferrite and iron oxide are primarily due to a greater reduction extent of the cobalt ferrite, which is transformed to a metal alloy (Figure 6b). It is particularly interesting that the spinel structure is able to reform upon oxidation of the ALD-$Co_{0.85}Fe_{2.15}O_4$ films. Mohan et al. proposed that $CoFe_2O_4$ can be synthesized by oxidation of $CoFe_2$,[46] and our observations support this hypothesis.

DISCUSSION AND CONCLUSIONS

Nanoscale (2−5 nm), conformal films of maghemite (γ-Fe_2O_3) and spinel cobalt oxides ($Co_xFe_{3-x}O_4$) deposited by ALD on porous m-ZrO_2 supports exhibit the ability to be cycled rapidly and repeatedly in chemical looping cycles for the production of H_2. This cycle is composed of a chemical reduction step using 1:1:2 H_2:CO:CO_2 followed by regeneration of the original oxide using steam. Inclusion of CO_2 as an oxidant in the reduction gas mixture is essential to eliminate the deactivation of ALD γ-Fe_2O_3 resulting from formation of metallic Fe. In situ XRD indicates that ALD γ-Fe_2O_3 is reduced to Fe^{2+} (FeO), while ALD-$Co_{0.85}Fe_{2.15}O_4$ is reduced completely to form a Co/Fe alloy. We find that ALD−$Co_{0.85}Fe_{2.15}O_4$ samples undergo little to no deactivation during cycling, in contrast to ALD γ-Fe_2O_3 films, which experience a substantial reduction of H_2 yield (>50% of the total H_2 production) and peak rate (>20%), respectively.

Of the two materials evaluated here, the cobalt ferrites are superior for several reasons. First, they can be fully reduced to metallic Co and Fe, resulting in much greater H_2 yields (about a factor of 4). Second, these materials are unaffected by up to seven redox cycles, which is encouraging with respect to long-term use. Finally, their H_2 production rates are substantially faster than those of powders (see discussion below), as a result of surfaces that are fully exposed to the gas, rather than a dense microcrystalline structure that is rate-limited by oxygen diffusion along grain boundaries or through the bulk.

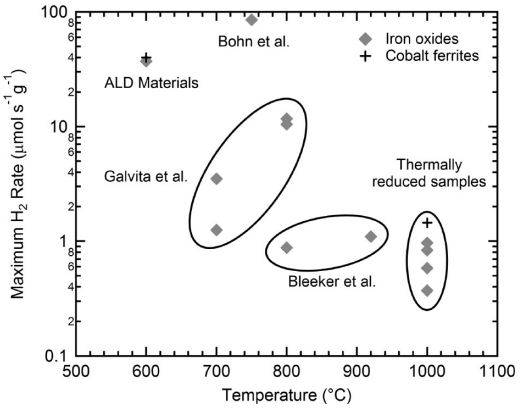

Figure 8. Peak H_2 rates as a function of temperature of ALD materials compared to others documented in the literature.

Because of the stability and high surface area of the ALD materials, their peak H_2 reaction rates are considerably higher than most chemically and thermally reduced materials with lower surface areas. A comparison of peak H_2 rates reported here with those for iron oxide and cobalt oxide based materials reported in

the literature is shown in Figure 8. Compared with thermally reduced iron oxide samples, the ALD γ-Fe_2O_3 rates are 38−100 times higher.[4,5,20,47] Data for thermally reduced cobalt ferrites are more sparse, but the results presented by Kodama et al. for thermally reduced (at 1400 °C) ZrO_2-supported cobalt ferrite are 28 times slower than the corresponding ALD rates,[5] even though the data were obtained at 1000 °C where faster kinetics are expected. This highlights the deleterious effect of high temperature sintering and grain growth, which shifts the rate-limiting step from surface kinetics to diffusion, either through the Fe_3O_4 product layer or along grain boundaries, both of which are much slower.[48,49]

Bleeker et al. also measured WS rates at 800 and 920 °C using a catalytic iron oxide having a surface area comparable to our ALD samples (31.2 $m^2\ g^{-1}$).[50] However, to prevent deactivation from sintering during cycling, the material was sintered prior to WS, leaving a surface area of only 0.05−0.1 $m^2\ g^{-1}$. As a result, the peak H_2 rates are 34 and 42 times lower at 800 and 920 °C, respectively, than ALD γ-Fe_2O_3. Similarly, Galvita et al. used 30 wt % Fe_2O_3 supported on $Ce_{0.5}Zr_{0.5}O_2$ with a surface area of 9.1 $m^2\ g^{-1}$,[51] obtaining peak rates at 800 °C approximately 10.5 μmol $s^{-1}\ g^{-1}$ for Fe_2O_3, or about 3.5 times lower than ALD γ-Fe_2O_3. However, when the temperature was decreased to 700 °C, their reaction rates decreased drastically to 3.5 and 1.25 μmol $s^{-1}\ g^{-1}$, suggesting a different rate-limiting process than in the ALD films. The peak rates of Bohn et al. at 750 °C are approximately two times greater than those presented here at 600 °C, even though their specific surface areas are much less than the ALD materials.[2] Fe_2O_3 particles <5 μm were used, but presintered to a particle size of 425−600 μm to prevent further sintering during cycling. Even so, after 5 cycles, their rates decrease by about 50%. Additionally, it should be noted that their rates were about 25 times less, on a per mass basis, when the mass of their packed bed was increased from 1 g to 20 g.

Together, these results suggest a path forward to durable materials that could be used in a variety of thermal redox and chemical looping cycles. Moreover, they show that ALD thin films are an attractive platform for probing fundamental reaction chemistry without the limitations imposed by transport through the bulk or along grain boundaries. The current support material used here (m-ZrO_2) is limited to temperatures ≤600 °C, but deposition on more thermally stable substrates could extend this stability range. We note that even though these films are very thin, the high surface area of the supports allows high oxide loadings (we achieved up to 37 wt %), showing that practical H_2 production rates are feasible with these materials. ALD processes for depositing a wide variety of materials are now available,[27,30,33,52] indicating this platform has considerable versatility. Finally, although our measurements of WS reaction kinetics on these materials are limited, they demonstrate that sintering can be largely eliminated, allowing the redox chemistry itself to be probed over multiple reaction cycles.

AUTHOR INFORMATION

Corresponding Author

*Phone: (925) 294-1440 (A.H.M.), (303) 492-3759 (A.W.W.). Fax: (925) 294-2276 (A.H.M.), (303) 492-4341 (A.W.W.). E-mail: amcdani@sandia.gov (A.H.M.), alan.weimer@colorado.edu (A.W.W.).

ACKNOWLEDGMENT

This work was supported by the Laboratory Directed Research and Development Sunshine to Petrol program at Sandia National Laboratories and the U.S. Department of Energy Fuel Cell Technologies Program via the Solar Thermochemical Hydrogen (STCH) directive. Sandia is a multiprogram laboratory operated by Sandia Corporation, a Lockheed Martin Company, for the United States Department of Energy's National Nuclear Security Administration under Contract DE-AC04-94AL85000.

REFERENCES

(1) Jin, H.; Okamoto, T.; Ishida, M. *Enery Fuels* **1998**, *12* 1272–1277.
(2) Bohn, C. D.; Muller, C. R.; Cleeton, J. P.; Hayhurst, A. N.; Davidson, J. F.; Scott, S. A.; Dennis, J. S. *Ind. Eng. Chem. Res.* **2008**, *47*, 7623–7630.
(3) Miller, J. E.; Allendorf, M. D.; Diver, R. B.; Evans, L. R.; Siegel, N. P.; Stuecker, J. N. *J. Mater. Sci.* **2008**, *43*, 4714–4728.
(4) Gokon, N.; Murayama, H.; Umeda, J.; Hatamachi, T.; Kodama, T. *Int. J. Hydrogen Energy* **2009**, *34*, 1208–1217.
(5) Kodama, T.; Kondoh, Y.; Yamamoto, R.; Andou, H.; Satou, N. *Sol. Energy* **2005**, *78*, 623–631.
(6) Fino, D.; Russo, N.; Saracco, G.; Specchia, V. *J. Catal.* **2006**, *242*, 38–47.
(7) Simonsen, V. L. E.; Find, D.; Lilliedal, M.; Petersen, R.; Kammer, K. *Top. Catal.* **2007**, *45*, 143–148.
(8) Silva, J. B.; Diniz, C. F.; Lago, R. M.; Mohallem, N. D. S. *J. Non-Cryst. Sol* **2004**, *348*, 201–204.
(9) Yang, Q.; Choi, H.; Al-Abed, S. R.; Dionysiou, D. D. *Appl. Catal., B* **2009**, *88*, 462–469.
(10) Uddin, M. A.; Tsuda, H.; Wu, S. J.; Sasaoka, E. *Fuel* **2008**, *87*, 451–459.
(11) Lee, J. Y.; Lee, D. W.; Lee, K. Y.; Wang, Y. *Catal. Today* **2009**, *146*, 260–264.
(12) Baldychev, I.; Vohs, J. M.; Gorte, R. J. *Appl. Catal., A* **2009**, *356*, 225–230.
(13) Yoon, T. J.; Lee, W.; Oh, Y. S.; Lee, J. K. *New J. Chem.* **2003**, *27*, 227–229.
(14) Bleeker, M. F.; Kersten, S. R. A.; Veringa, H. J. *Catal. Today* **2007**, *127*, 278–290.
(15) Bleeker, M. F.; Veringa, H. J.; Kersten, S. R. A. *Appl. Catal., A* **2009**, *357*, 5–17.
(16) Loutzenhiser, P. G.; Galvez, M. E.; Hischier, I.; Stamatiou, A.; Frei, A.; Steinfeld, A. *Energy Fuels* **2009**, *23*, 2832–2839.
(17) Weidenkaff, A.; Nuesch, P.; Wokaun, A.; Reller, A. *Solid State Ionics* **1997**, *101*, 915–922.
(18) Hossain, M. M.; Lopez, D.; Herrera, J.; de Lasa, H. I. *Catal. Today* **2009**, *143*, 179–186.
(19) Zafar, Q.; Mattisson, T.; Gevert, B. *Energy Fuels* **2006**, *20*, 34–44.
(20) Kodama, T.; Nakamuro, Y.; Mizuno, T. *J. Sol. Energy* **2006**, *128*, 3–7.
(21) Huang, W.; Zhou, L. X.; Zeng, H. Z.; Wei, X. H.; Zhu, J.; Zhang, Y.; Li, Y. R. *J. Cryst. Growth* **2007**, *300*, 426–430.
(22) Echigoya, J.; Asano, W.; Yamaguchi, A. *Phys. Status Solidi A* **2002**, *191*, 359–369.
(23) Bahlawane, N.; Ngamou, P. H. T.; Vannier, V.; Kottke, T.; Heberle, J.; Kohse-Hoinghaus, K. *Phys. Chem. Chem. Phys.* **2009**, *11*, 9224–9232.
(24) Lim, B. S.; Rahtu, A.; Gordon, R. G. *Nat. Mater.* **2003**, *2*, 749–754.
(25) Rooth, M.; Lindahl, E.; Harsta, A. *Chem. Vap. Deposition* **2006**, *12*, 209–213.
(26) Klepper, K. B.; Nilsen, O.; Fjellvag, H. *J. Cryst. Growth* **2007**, *307*, 457–465.
(27) Klepper, K. B.; Nilsen, O.; Fjellvag, H. *Thin Solid Films* **2007**, *515*, 7772–7781.
(28) de Ridder, M.; van de Ven, P. C.; van Welzenis, R. G.; Brongersma, H. H.; Helfensteyn, S.; Creemers, C.; Van Der Voort, P.;

Baltes, M.; Mathieu, M.; Vansant, E. F. *J. Phys. Chem. B* **2002**, *106*, 13146–13153.
(29) Nilsen, O.; Lie, M.; Foss, S.; Fjellvag, H.; Kjekshus, A. *Appl. Surf. Sci.* **2004**, *227*, 40–47.
(30) Lie, M.; Fjellvag, H.; Kjekshus, A. *Thin Solid Films* **2005**, *488*, 74–81.
(31) Bachmann, J.; Jing, J.; Knez, M.; Barth, S.; Shen, H.; Mathur, S.; Gosele, U.; Nielsch, K. *J. Am. Chem. Soc.* **2007**, *129*, 9554–9555.
(32) Rooth, M.; Johansson, A.; Kukli, K.; Aarik, J.; Boman, M.; Harsta, A. *Chem. Vap. Deposition* **2008**, *14*, 67–70.
(33) Scheffe, J. R.; Frances, A.; King, D. M.; Liang, X. H.; Branch, B. A.; Cavanagh, A. S.; George, S. M.; Weimer, A. W. *Thin Solid Films* **2009**, *517*, 1874–1879.
(34) Lie, M.; Klepper, K. B.; Nilsen, O.; Fjellvag, H.; Kjekshus, A. *Dalton Trans.* **2008**, 253–259.
(35) King, D. M.; Spencer, J. A.; Liang, X.; Hakim, L. F.; Weimer, A. W. *Surf. Coat. Technol.* **2007**, *201*, 9163–9171.
(36) Leskela, M.; Ritala, M. *Thin Solid Films* **2002**, *409*, 138–146.
(37) Chernyshova, I. V.; Hochella, M. F.; Madden, A. S. *Phys. Chem. Chem. Phys.* **2007**, *9*, 1736–1750.
(38) Gehring, A. U.; Fischer, H.; Louvel, M.; Kunze, K.; Weidler, P. G. *Geophys. J. Int.* **2009**, *179*, 1361–1371.
(39) Navrotsky, A.; Mazeina, L.; Majzlan, J. *Science* **2008**, *319*, 1635–1638.
(40) Sakurai, S.; Namai, A.; Hashimoto, K.; Ohkoshi, S.-i. *J. Am. Chem. Soc.* **2009**, *131*, 18299–18303.
(41) Jacintho, G. V. M.; Brolo, A. G.; Corio, P.; Suarez, P. A. Z.; Rubim, J. C. *J. Phys. Chem. C* **2009**, *113*, 7684–7691.
(42) Bale, C.; Chartrand, P.; Degterov, S. A.; Eriksson, G.; Hack, K.; Ben Mahfoud, R.; Melancon, J.; Pelton, A. D.; Petersen, S. *Calphad* **2002**, *26*, 189–228.
(43) Lu, Z. G.; Zhu, J. H.; Bi, Z. H.; Lu, X. C. *J. Power Sources* **2008**, *180*, 172–175.
(44) Ustinovshikov, Y. I.; Pushkarev, B. E.; Sapegina, I. V. *Inorg. Mater.* **2006**, *42*, 354–359.
(45) Orfao, J. J. M.; Martins, F. G. *Thermochim. Acta* **2002**, *390*, 195–211.
(46) Mohan, M.; Chandra, V.; Manoharan, S. S. *J. Mater. Res.* **2008**, *23*, 1849–1853.
(47) Gokon, N.; Murayama, H.; Nagasaki, A.; Kodama, T. *Sol. Energy* **2009**, *83*, 527–537.
(48) Atkinson, A.; Odwyer, M. L.; Taylor, R. I. *J. Mater. Sci.* **1983**, *18*, 2371–2379.
(49) Tinkler, S.; Dieckmann, R. *J. Mater. Sci.* **1992**, *27*, 3799–3802.
(50) Bleeker, M. F.; Veringa, H. J.; Kersten, S. R. A. *Ind. Eng. Chem. Res.* **2010**, *49*, 53–64.
(51) Galvita, V.; Sundmacher, K. *Appl. Catal., A* **2005**, *289*, 121–127.
(52) Hakim, L. F.; George, S. M.; Weimer, A. W. *Nanotechnology* **2005**, *16*, S375–S381.

■ NOTE ADDED AFTER ASAP PUBLICATION

This article was published ASAP on March 24, 2011, with an error in the Abstract and Table of Contents graphics. The corrected version was published ASAP on March 30, 2011.